



A high performance field-reversed configuration^{a)}

M. W. Binderbauer,^{1,b)} T. Tajima,¹ L. C. Steinhauer,¹ E. Garate,¹ M. Tuszewski,¹ L. Schmitz,^{1,2} H. Y. Guo,^{1,3} A. Smirnov,¹ H. Gota,¹ D. Barnes,¹ B. H. Deng,¹ M. C. Thompson,¹ E. Trask,¹ X. Yang,¹ S. Putvinski,¹ N. Rostoker,¹ R. Andow,¹ S. Aefsky,¹ N. Bolte,¹ D. Q. Bui,¹ F. Ceccherini,¹ R. Clary,¹ A. H. Cheung,¹ K. D. Conroy,¹ S. A. Detrick,¹ J. D. Douglass,¹ P. Feng,¹ L. Galeotti,¹ F. Giannamico,⁴ E. Granstedt,¹ D. Gupta,¹ S. Gupta,¹ A. A. Ivanov,⁵ J. S. Kinley,¹ K. Knapp,¹ S. Korepanov,¹ M. Hollins,¹ R. Magee,¹ R. Mendoza,¹ Y. Mok,¹ A. Necas,¹ S. Primavera,¹ M. Onofri,¹ D. Osin,¹ N. Rath,¹ T. Roche,¹ J. Romero,¹ J. H. Schroeder,¹ L. Sevier,¹ A. Sibley,¹ Y. Song,¹ A. D. Van Drie,¹ J. K. Walters,¹ W. Waggoner,¹ P. Yushmanov,¹ K. Zhai,¹ and TAE Team

¹Tri Alpha Energy, Inc., P.O. Box 7010, Rancho Santa Margarita, California 92688, USA

²Department of Physics and Astronomy, University of California at Los Angeles, Los Angeles, California 90095-1547, USA

³General Atomic, P.O. Box 85608, San Diego, California 92186-5608, USA

⁴Department of Physics, University of Pisa, Largo B. Pontecorvo 3, 56127 Pisa, Italy

⁵Budker Institute of Nuclear Physics, 11 Lavrentyev Avenue, 630090 Novosibirsk, Russia

(Received 21 November 2014; accepted 23 February 2015; published online 15 May 2015)

Conventional field-reversed configurations (FRCs), high-beta, prolate compact toroids embedded in poloidal magnetic fields, face notable stability and confinement concerns. These can be ameliorated by various control techniques, such as introducing a significant fast ion population. Indeed, adding neutral beam injection into the FRC over the past half-decade has contributed to striking improvements in confinement and stability. Further, the addition of electrically biased plasma guns at the ends, magnetic end plugs, and advanced surface conditioning led to dramatic reductions in turbulence-driven losses and greatly improved stability. Together, these enabled the build-up of a well-confined and dominant fast-ion population. Under such conditions, highly reproducible, macroscopically stable hot FRCs (with total plasma temperature of ~ 1 keV) with record lifetimes were achieved. These accomplishments point to the prospect of advanced, beam-driven FRCs as an intriguing path toward fusion reactors. This paper reviews key results and presents context for further interpretation. © 2015 AIP Publishing LLC. [<http://dx.doi.org/10.1063/1.4920950>]

I. INTRODUCTION AND MOTIVATION

A field-reversed configuration (FRC) is a high-beta, prolate compact toroid (CT) embedded in a predominantly self-generated poloidal axisymmetric magnetic field with little or no toroidal field.^{1,2} The engineering beta value of these topologies is near unity, i.e., $\langle \beta \rangle = 8\pi \langle p \rangle / B_e^2 \sim 1$, where $\langle p \rangle$ is the average plasma pressure and B_e the externally applied magnetic field. In principle, this permits a compact reactor with high power density. Moreover, the low interior magnetic field provides for a considerable indigenous fraction of large orbit particles and enables the capability to burn aneutronic fuels. Since the FRC topology is generated by the plasma's own diamagnetic currents of sufficient strength to reverse the forward magnetic field, the configuration only requires solenoidal coils located outside of a simply connected pressure vessel. This elegant geometry greatly facilitates engineering and maintenance. Furthermore, the core plasma is enclosed by a scrape-off-layer (SOL) that coalesces into axial jets beyond each end of the FRC and forms a natural linear divertor. This allows for convenient unrestricted removal of power (possibly with direct conversion to electricity), ash, and impurities. Further, FRCs can be readily

translated, collided, and merged,³ permitting convenient separation of formation and burn regions, which in turn promotes the most optimized engineering solutions and material choices for each.

As an improvement upon conventional FRCs, advanced beam driven FRCs have been proposed as a means to improve the confinement and stability.^{4,5} The rationale rests on the conjecture that energetic large orbit particles are mostly immune to micro-turbulence driven transport and provide a stiffening effect that improves macro-stability as well.^{6–10} An essential ingredient for achieving this High Performance Field-reversed configuration (HPF) state is the tangential injection and retention of fast ions via neutral beams (NBs) to produce significant fast-ion pressure, comparable to the thermal plasma pressure. This concept can naturally extend to an envisioned reactor where the beams also contribute to current drive, plasma heating, and fueling.

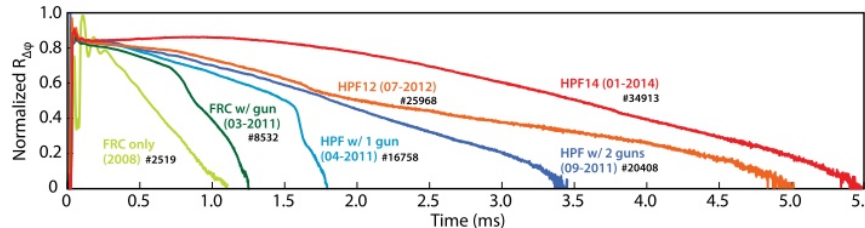
These aggregate advantages have motivated a long-standing interest in developing the FRC towards a compact magnetic fusion reactor with neither toroidal field coils nor a central solenoid. Broad-based reviews have mapped pathways and milestones towards this goal. In the recent past, two US Department of Energy-sponsored studies outlined scientific issues needing resolution in toroidal systems, including the FRC, namely, the Toroidal Alternates Panel report (2008) and the Research Needs Workshop (2009).^{11,12}

^{a)}Paper VI2 1, Bull. Am. Phys. Soc. **59**, 361 (2014).

^{b)}Invited speaker.

056110-2 Binderbauer *et al.*

Phys. Plasmas 22, 056110 (2015)



Relative to the FRC, these studies defined scientific goals to be achieved within about two decades. The FRC relevant goal was summarized as “demonstrating that a compact toroid with simply connected vessel can achieve a stable, long-pulsed plasma at kilovolt temperatures with favorable confinement scaling to proceed to a pre-burn CT plasma experiment.” These studies recognized this as a highly ambitious objective, requiring notable extrapolations in stability, confinement, and sustainment, in short “new physics.” In particular, five scientific challenges were identified: (1) Understand global stability at low collisionality with large $S \sim R_s/\rho_i \geq 30$ (FRC radius \div Larmor radius in the external field), (2) measure and identify the energy transport process and ascertain whether it has favorable scaling to high temperatures, (3) establish the viability of energy-efficient sustainment at large S consistent with good confinement, (4) overcome theory and simulation challenges posed by high-beta and kinetic (large orbit) effects, including any connection to the anomalous transport in early experiments, (5) develop a mature diagnostics capability, overcoming the unique challenges in adapting existing tools. To address these challenges, the studies recommended construction and operation of a larger-size, well-diagnosed FRC research facility capable of current drive and heating by rotating magnetic fields (RMFs) or neutral beams.

At about the same time as the foregoing scientific challenges were identified, Tri Alpha Energy (TAE) embarked on early experiments on C-2, its then new beam-driven FRC facility.³ C-2 was designed as a test bed for studying basic questions related to beam-driven FRC physics. It is, therefore, no great surprise that most of the issues highlighted by the two studies resembled key objectives for C-2. Indeed, the only issues not planned for investigation in C-2 were large-S behavior and rotating magnetic field current drive. Instead, C-2 focused toward a small-S FRC reactor manifestation, in line with the inherent advantages⁶ of highly kinetic FRCs driven by neutral beam injection (NBI). In particular, C-2’s key objectives were

- (1) Design for a rapid learning cycle, i.e., high shot rates (discharges every ≤ 10 min) so as to enhance physics learning via development of a large experimental database (to date over 40 000 discharges on C-2).
- (2) Achieve plasma lifetimes longer than 5 ms with high reproducibility. The intent was to exceed all relevant time scales, such as confinement and charge-exchange times, as well as possible instability growth times. Again, repeatability is essential for efficient data interpretation.
- (3) Apply tangential NBI and develop an understanding of fast particle effects on stability and transport, consistent with the central tenet of TAE’s concept.
- (4) Generate macro-stable FRCs to enable the effective study of transport properties and the potential for sustainment.
- (5) Measure fluctuations and consequent transport rates to establish the scaling behavior of NB-driven FRCs in the highly kinetic regime.
- (6) Characterize current drive and power balance with implications towards a potential future reactor.
- (7) Tightly integrate theory and modeling with experimentation to enhance physics understanding.
- (8) Develop the essential engineering knowhow and integration in anticipation of future steps.
- (9) Accelerate the entire project from design and construction to operation and knowledge generation by enlisting and supporting global collaborations; to date, TAE enjoys productive collaborations with many leading plasma physics institutions, domestic and international.

During a half-decade or so of experimentation on C-2, dramatic advances were made in formation and overall operation of beam-driven hybrid FRCs, as well as in confinement and stability. Figures 1 and 2 illustrate some of the key advances made on C-2. Figure 1 summarizes the improvement in the lifetime of the plasma diamagnetism over the course of the C-2 experiments, from late 2008 to early 2014. Plotted is the normalized excluded flux radius of the plasma (approximating the separatrix radius) versus discharge time. The notable improvements correlate with distinct operational conditions, distinguished by different equipment and operating techniques, such as edge biasing, neutral beams, and gettering agents. The slope of the mostly decaying traces is proportional to the overall loss rate, and shows a clear flattening and smoothing as the operational methodology advanced, reflecting improvements in confinement and stability. Observe that the trace labeled “HPF14” exhibits a temporary phase (up to 1 + ms) where the radius actually

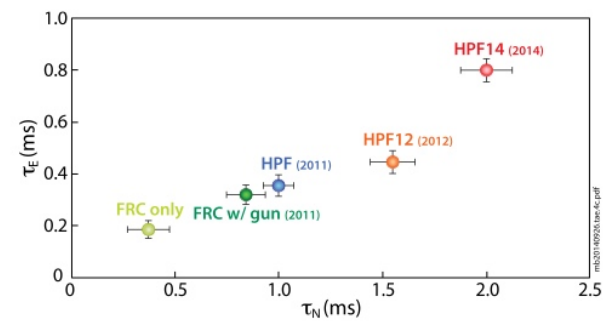


FIG. 2. Improvements in total energy and particle confinement times.^{13–16}

increases. This is consistent with a sustained flux profile for up to 1 ms, and looks especially promising for a future sustainment experiment. Correlated with that is a parallel improvement in global energy and particle confinement times, as detailed in Fig. 2. Again, the positive evolution clearly correlates with improving, but distinct experimental regimes. Each data point is ensemble-averaged over many shots with error bars indicating the data spread. Notice that the latest (2014) data point shows a stronger improvement in energy relative to particle confinement, indicating an additional reduction in non-convective thermal losses.

Overall, successful operation of the C-2 FRC facility demonstrates mastery of FRC formation via fast collisional merging, long-lifetime plasma evolution, the benefits of fast ions from NBI, and the engineering integration of major subsystems.^{3,13} More importantly, extensive performance optimization led to the discovery of the HPF regime,^{14,15} which is achieved by a synergistic interaction between edge-biasing, neutral beams (and the fast ion population it creates) and surface gettering. The main characteristics of the HPF regime include: (1) macroscopically stable discharges (lifetime only limited by transport), (2) excellent shot-to-shot reproducibility, (3) dramatically reduced transport rates (up to an order of magnitude lower than the non-HPF regime), (4) minimized radiative losses, (5) record diamagnetism lifetimes (exceeding 5 ms), (6) coupled FRC-core-to-SOL transport paradigm (a double transport barrier, intercoupling core and SOL physics), and (7) emerging global energy confinement scaling with strongly favorable temperature dependence. Together these achievements anticipate sustainment techniques to be exploited and further enhanced in future TAE facilities. Heating, current drive, and overall sustainment appear to be within reach by a selective upgrade of C-2's current capabilities.

This paper, summarizing key C-2 results, is organized as follows. Section II A is a brief overview of the machine design. Section II B discusses formation from separate theta-pinch sources to collisional merging in the central confinement chamber, while Sec. II C describes equilibrium characteristics of this FRC, now a suitable target for NBI.

Section II D summarizes fast-ion effects, followed by an overview of stability and confinement in Secs. II E and II F, respectively. Section III briefly introduces near-future next steps and associated goals. Finally, Sec. IV presents a summary and conclusions.

II. PHYSICS ADVANCES ON C-2

A. Machine design and key components

Figure 3 depicts a schematic of the C-2 facility. It consists of a central confinement region (~4 m long, ~0.7 m radius metal wall), interposed between two CT formation sections (~4 m length, ~0.4 m radius quartz wall). At each end are divertor chambers (~2 m length, ~0.7 m radius metal wall) to control neutrals and impurities. The stainless steel confinement chamber approximately conserves magnetic flux on the timescale of the experiment. The formation systems, with quartz tubes, are based on a variant of the field-reversed theta-pinch method, albeit with an advanced pulsed power system that allows for dynamic formation.³ Both divertors house coaxially mounted plasma guns of the AMBAL type^{17,18} as well as concentric ring electrode sets for edge biasing and radial electric-field control.

A series of magnets, placed along the length of the device, generate a quasi-static axial magnetic field, B_z , throughout. Some of the coils provide the external magnetic-field essential for radial equilibrium in the central section. Higher-field "mirror" coils between the central and formation sections contribute to axial equilibrium. Others provide the bias field in the formation sections and, past formation, the necessary field to guide the end-streaming plasma jets into the divertor chambers. The typical field strength in the central section is $B_z \sim 1$ kG, with the mirror coils creating a mirror ratio of ~ 3.5 . Formation-section bias fields, B_{FS} , typically operate in the 0.5–1.1 kG range. In addition, there are magnetic "mirror-plugs" (i.e., "plug" mirror coils) between the formation and divertor sections that can produce strong magnetic fields (B_{plug}) up to ~ 20 kG, a plug-mirror-ratio ($R_p = B_{plug}/B_z$) up to ~ 20 . The mirror-plugs play an important role in reducing the particle end loss from the SOL, as

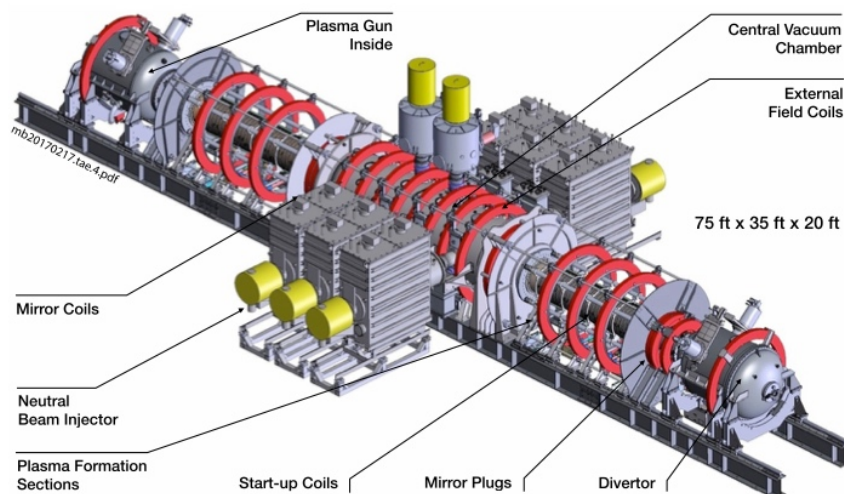


FIG. 3. Schematic of the C-2 facility and main components.

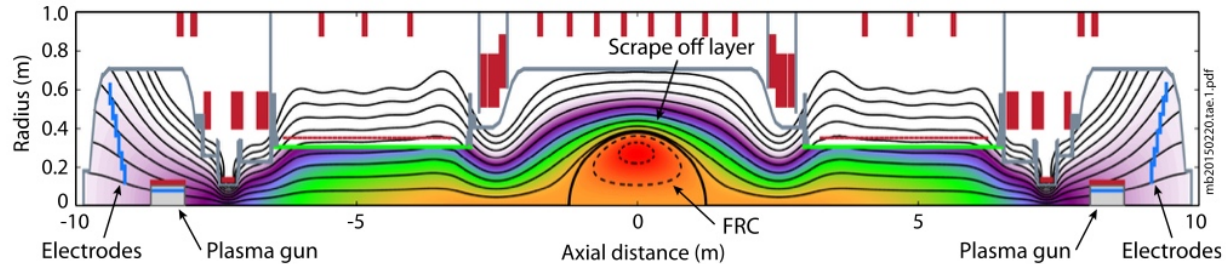


FIG. 4. Depiction of a poloidal slice (r - z cylindrical coordinates) of C-2 showing field surface contour lines and plasma density (color), calculated by a 2-D magnetohydrodynamic (MHD) numerical simulation using the LamyRidge equilibrium code.¹⁹

will be discussed. They are also effective for reducing neutral-gas backflow from the divertor chambers. Figure 4 illustrates computed magnetic flux and density contours during the equilibrium phase of C-2 operation.

In order to reduce the impurity concentration and control recycling, C-2 was outfitted with titanium and/or lithium gettering systems. These provide line-of-sight wall coating capability for about 80% of the inner surface area of the central and end divertor sections. Reducing the neutral load in the peripheral regions is critical for trapping and long-time retention of injected fast ions, since a large portion of their trajectory paths lies in the periphery. In a typical C-2 discharge without gettering, the dominant impurities are oxygen, carbon, and nitrogen, mainly from the chamber walls and formation sections. Both Ti and Li-gettering have significantly reduced neutral recycling (based on D_{α} emissions at $\lambda \sim 656$ nm) by a factor of 4–5 compared to shots without wall conditioning.²⁰ In addition, survey spectrometry of gettered shots also indicates a large reduction in impurity concentration. Indeed, recent measurements with optimal HPF operation and lithium wall coating reveal a very clean core plasma with $Z_{\text{eff}} \sim 1.28$.²¹

AMBAL-type plasma-guns are mounted coaxially in each divertor, as illustrated in Fig. 4. These generate a warm (electrons $T_e \sim 30$ –50 eV, ions $T_i \sim 100$ eV), tenuous ($n_e < 10^{19} \text{ m}^{-3}$) plasma stream. The typical anode-to-cathode voltage difference is ~ 500 V and the gun arc-current is ~ 10 kA. The guns perform multiple functions: (1) create an inward radial electric field in the SOL¹⁵ (important for $n = 2$

rotational stability), (2) establish electromagnetic shear in the SOL (effective to suppress local fluctuations), and (3) tightly center the plasma (less $n = 1$ wobble motion) via lining-tight to the gun electrodes.

C-2 is outfitted with up to eight NBs (20–40 keV hydrogen, ~ 4 MW total), distributed around the azimuth and along the central section of the machine, as illustrated in Fig. 3.²² All beams are injected perpendicular to the confinement chamber and aimed in the ion-diamagnetic drift direction along a chord that misses the axis by ~ 0.19 m (impact parameter). The fast ions, created by charge exchange, trace out large-scale betatron orbits that contribute to the plasma current and build up a fast-ion population with pressure eventually comparable to the thermal pressure. In HPF operations, these conditions produce efficient NB injection with shine-through and first orbit losses under 15% during the early part of the discharge.

Table I summarizes the C-2 diagnostics, a comprehensive suite²³ of over 60 individual systems on 137 vessel ports and recording well over 1000 channels of data from every discharge. These include, among others, time- and space-resolved Thomson scattering,²⁴ CO₂/HeNe²⁵ and dispersion²⁶ based interferometry, magnetic diagnostics,²⁷ assorted spectroscopic systems (charge-exchange recombination spectroscopy,²⁸ D _{α} /H _{α} ,²⁹ Doppler,³⁰ vacuum ultraviolet³¹ and survey spectrometers), bolometry,³² fast ion diagnostics (including neutral particle analyzers (NPAs),³³ neutral particle bolometer arrays,³⁴ neutron detectors,³⁵ proton detectors³⁶), polarimetry

TABLE I. C-2 diagnostics suite.

Shape/position	Densities/fluctuation	Temperatures/radiation	Fast ions/neutrals
Formation B _{z} probes	CO ₂ interferometer	Thomson scattering	Electrostatic NPA
Formation flux loops	Visible He-Ne interferometer	Soft X-ray detector	Electromagnetic NPAs
Confinement B _{z} probes	IR He-Ne interferometer	Line ratio spectrometer	Neutral particle bolometer
Confinement B _{θ} probes	Dispersion interferometers	He-jet Mach nozzle	Pyro bolometers
Mirnov probe arrays	Microwave interferometers	Fast Doppler spectrometer	SEE detectors
Internal B probe arrays	Cut-off reflectometer	High resolution Doppler	ZnS scintillator
Polarimeter	Fluctuation reflectometer	Survey spectrometers	Plastic scintillators
CCD end cameras	Fluctuation imaging	IR spectrometer	Beam H _{α} analyzer
X-ray imaging cameras	Triple probe	Impurity line monitors	Modulated H beam
Bremsstrahlung arrays	Mach probe	VUV spectrometer	D _{α} monitors
Video camera	Rake probe	He-3 neutron counters	D _{α} /D _{β} intensity ratios
	Gundestrup probe	Ion energy analyzer	Pellet CCD camera
	Particle flux probe	Bolometer arrays	Fast ionization gauges
	Plasma potential probe	End-on bolometer	RGAs

056110-5 Binderbauer *et al.*

Phys. Plasmas 22, 056110 (2015)

for magnetic profiles and via far-infrared (FIR) laser-based forward-scattering density fluctuations measurements,³⁷ reflectometry for density and fluctuation imaging,³⁸ as well as a host of plasma probes.³⁹ These systems provide corroborated methods to interpret many details from experiments: (1) structure and evolution of the density, temperature, and magnetic field profiles; (2) bulk plasma motion and shape evolution; (3) temporal and spatial resolution of impurity concentrations and plasma flows; (4) imaging of fluctuations in the core, over the plasma surface, and into the SOL; (5) detailed time- and space-resolved fast-ion behavior; as well as a host of other inferences. In addition, there are over 10 000 streams of engineering data that cover all operational aspects of the machine during, before, and after a discharge. The entire data acquisition system is fully integrated with the control system and almost all discharge data are automatically post-processed within minutes following a shot and logged in a customized MDSplus tree and associated relational database. Aside from interpreting present experimental results, these data may be amenable and important for further knowledge discovery and devising possible feedback control.

B. Initial FRC formation

Large FRCs are produced in C-2 by collision merging of two CTs.^{3,13} Figure 5 shows the evolution of the excluded flux radius obtained from a magnetic probe array in the θ -pinch formation and central sections. Time is measured from the instant of field reversal in the θ -pinches, and distance is relative to the system midplane. Multi-gigawatt pulsed-power modules drive the θ -pinches, briefly reversing the magnetic field to ~ -0.5 kG, then raising it forward to ~ 0.4 kG, with field-reversal occurring by $t \sim 5$ μ s. The two CTs so formed then accelerate out of their respective θ -pinches at supersonic speeds, $v_z \sim 250$ km/s, and collide at

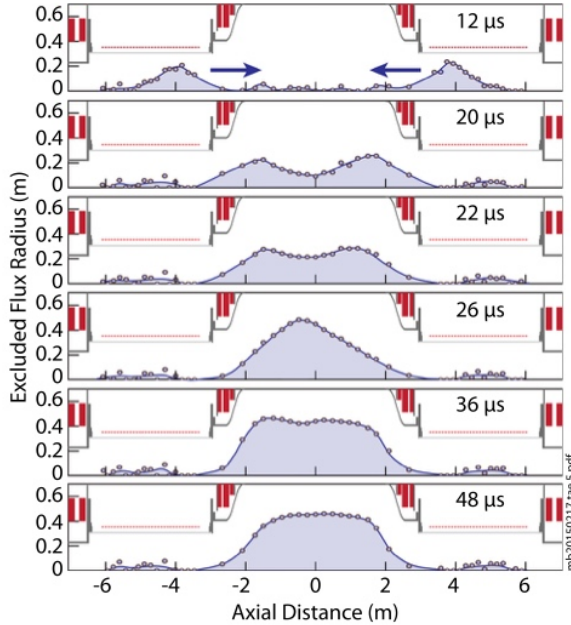


FIG. 5. Evolution of the excluded flux profile during formation.

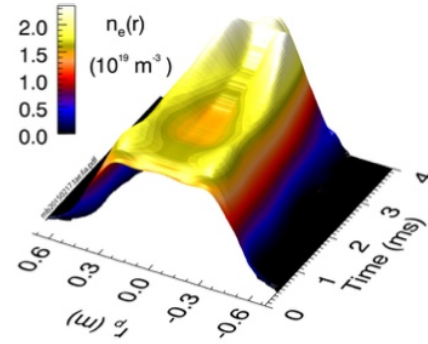


FIG. 6. Evolution of the near-midplane electron density profile of a recent HPF discharge as obtained from a six cord CO₂ interferometer.

the system mid-plane at about $t \sim 30$ μ s. The highly dynamical collision leads to rapid merging into an FRC with a natural lifetime of ~ 1 ms, in the absence of subsequent NB injection. The ~ 20 kJ kinetic energy of the two CTs thermalizes during the collision and merging process via shock heating, largely of the ions. In typical HPF discharges, an FRC thermal energy of ~ 7 kJ is retained post merging with total temperature $T_i + T_e \sim 1$ keV and $T_i/T_e \sim 4.5\text{--}5$. Note that the pre-merging CTs contain a significant toroidal magnetic field, a fraction of which may survive in the merged state.⁴⁰

C. Equilibrium characteristics and profiles

Typical C-2 bulk equilibrium parameters at $t \sim 500$ μ s, long after the merging, are the: separatrix radius $R_s \sim 0.35$ m, separatrix half-length $Z_s \sim 1.5$ m, poloidal flux up to $\Phi_P \sim 10$ mWb (rigid-rotor approximation), external axial magnetic field up to $B_e \sim 0.1$ T, average density up to $n_e \sim 3 \times 10^{19}$ m⁻³, total temperature in the range of 0.7 to 1 keV (electron temperature $T_e \sim 120$ eV). The plasma lifetimes without NB injection are typically ~ 1 ms, with the FRC separatrix shrinking radially and axially, and the temperature gradually decreasing. Figures 6 and 7 portray the evolution of experimental radial profiles near the mid-plane of the

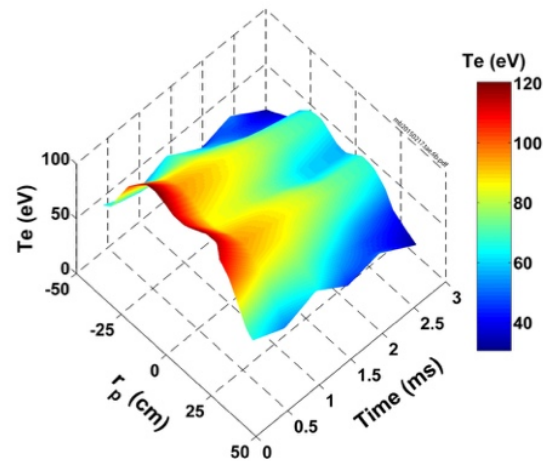


FIG. 7. Evolution of the near-midplane electron temperature profile, assembled out of an ensemble of recent HPF discharges, as obtained from a nine-point multi-pulse Thomson scattering system.

056110-6 Binderbauer *et al.*

Phys. Plasmas 22, 056110 (2015)

electron density and temperature, respectively.^{13,41} The density profile is based on Abel inverted CO₂ interferometry data, while the temperature profile is derived from Thomson scattering data. These equilibrium profiles are consistent with other FRC experiments and exhibit a hollow “double hump” structure across the diameter, characteristic of an FRC. Right after merging, the profiles are flat to slightly hollow, with more gentle gradients at the separatrix. They evolve toward a deeper hollow with steeper edge gradients.

Two key features of C-2 have a notable impact on the equilibrium, fast ions and finite SOL thickness as shown in Fig. 8.⁴² Except for the Thomson scattering data, the results come from C-2’s most recent HPF campaign. First, the total temperature, $T_i = T_i + T_e$, as derived from pressure balance is plotted assuming both a full rigid-rotor profile (black curve, labeled “w/SOL”) and a rigid-rotor truncated at the separatrix (solid black curve, labeled “no SOL”). Notably, accounting for the SOL raises the inferred pressure-balanced temperature by ~25%. Second, a direct measurement of the two temperatures, thermal-ion (ion Doppler spectroscopy), and electrons (Thomson scattering) leads to a somewhat lower total temperature (blue dashed curve). The difference between the pressure balance temperature (w/SOL) and the direct measurement total temperature is evidence of the significant current carried by fast ions and their consequent contribution to the total pressure.

Low neutral edge densities are important in all magnetic fusion concepts, but especially critical for beam-driven FRCs. In C-2, 20 keV fast ions produced by NB injection have large betatron orbits extending well outside the FRC proper with radial turning points at ~55 cm. Minimizing charge-exchange losses of these beam ions requires very low neutral densities in this peripheral region. C-2 employs fans of filtered fibers to collect the radial D_α emission profile, which can be Abel inverted; this, combined with the electron density profile (Fig. 6), yields the neutral density profile. This procedure is also benchmarked against numerical profiles derived from the well-known DEGAS2 code.⁴³ Careful vacuum practices combined with Li- and/or Ti-gettering have reduced neutral edge densities to insignificant levels as

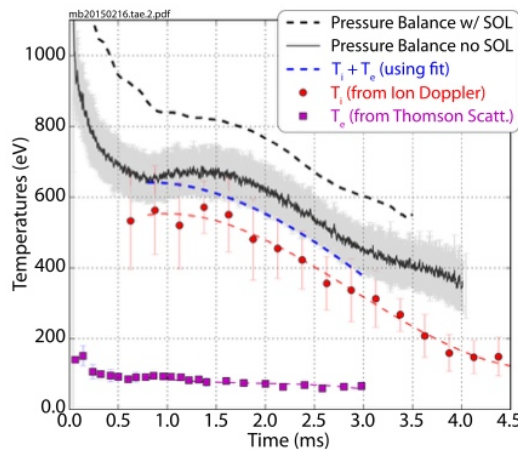


FIG. 8. Recent near mid-plane HPF ion and electron temperature histories.

demonstrated in Fig. 9. The figure shows the neutral density profile in the peripheral region, $r > 0.35$ m at a time $t = 1.2$ ms when $R_s \sim 0.3$ m. Also shown for comparison is the electron density in the peripheral region (thin blue line).

D. Fast ion effects

The primary goal of the C-2 experiments is to develop the physics of advanced beam driven FRCs. Extensive experimental and computational evidence elsewhere has shown that superthermal ions slow down and diffuse classically, even in the presence of turbulent fluctuations that drive anomalous transport of the thermal plasma (see, for instance, discussion and references in Ref. 6). If classical behavior also applies in C-2 (and in the absence of fast depopulating effects such as charge exchange, topological asymmetries, or stochastic diffusion^{16,44}), then NB injection will establish, within a few classical ion-electron scattering times, a slowing down distribution of fast ions that will help to sustain, stabilize, and reduce transport losses of the aggregate FRC plasma. Given the critical importance of these effects, C-2 was outfitted with multiple fast-ion diagnostics, and ample campaign time was devoted to study fast-ion effects on overall lifetime, confinement, and stability. Other efforts addressed fast-ion impact on the decay of the poloidal flux, as well as heating of electrons, the latter since fast ions predominantly heat electrons at the typical C-2 electron energy of ~100 eV. Although the overall NB power coupled to the plasma (~2.5 MW) is insufficient to balance energy losses (~3.5–4 MW in the latest HPF14 regime midway through the discharge), clear signatures have appeared showing the positive impact of fast ions from many experimental observations and consistent with numerical simulations.⁴⁴ One such effect is the temporary (~1 ms) rise in the ion temperature (ion Doppler) appearing in Fig. 8 (electron heating is also observed).

Fast-ion slowing down in C-2 is derived from beam-termination experiments. These results, shown in Fig. 10, are consistent with classical Coulomb scattering (i.e., $\tau \propto T_e^{3/2}/n_e$). The lifetime reported here is derived from the decay tails

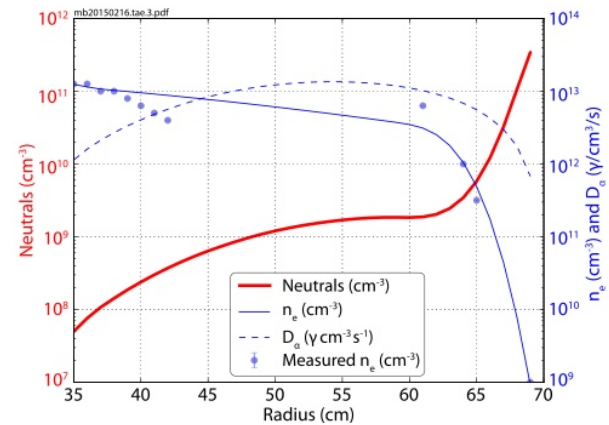


FIG. 9. Representative edge radial neutral density profile (bold red curve) in HPF14 Li-gettered discharges at 1.2 ms. Also shown is the D_α emission (dashed blue curve) used in deriving the neutral density.

056110-7 Binderbauer *et al.*

Phys. Plasmas 22, 056110 (2015)

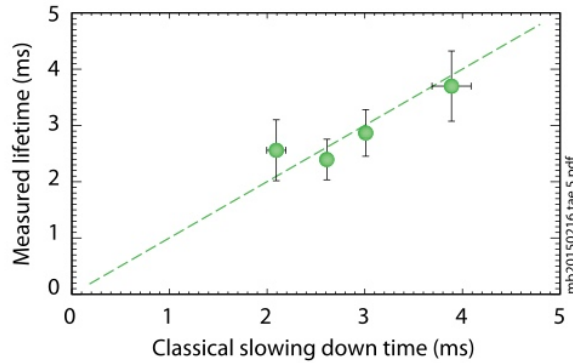


FIG. 10. Fast ion lifetime derived from beam termination experiments.

of neutron counts obtained from beam blip experiments with 15 keV deuteron-fueled neutral beams. It is also notable that the energy dependence of the slowing down time for higher-energy ions is consistent with increased charge-exchange losses, suffered from encountering higher neutral concentrations due to larger radial excursions. Based on all present data, D ions below 15 keV and H ions below 30 keV appear to be classically confined in C-2 HPF discharges.

Consider global effects of the fast-ion population, where clear performance gains accrue with increasing NB power. Figure 11 shows the improvement in diamagnetic lifetime with increased NB power, as evidenced by the slower temporal decay of the excluded flux radius. Each trace represents the average over an ensemble of similar HPF discharges, differing only in the beam power. Figure 12 shows the

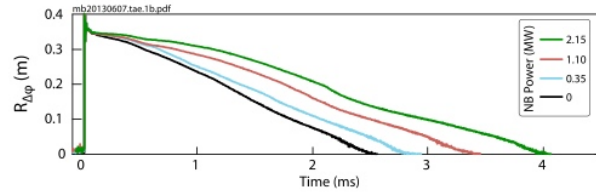


FIG. 11. Dependence of the diamagnetic plasma lifetime, represented by the decay of the excluded flux radius, on injected NB power.

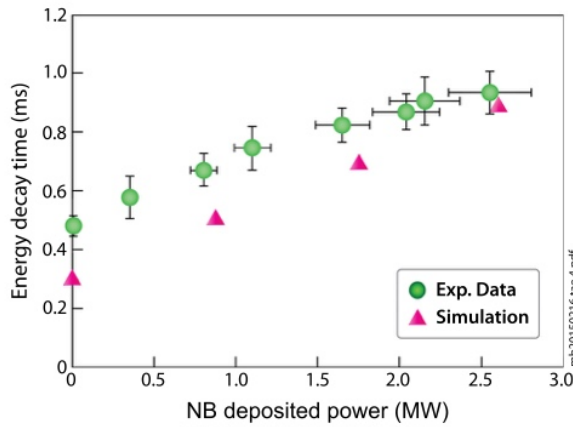
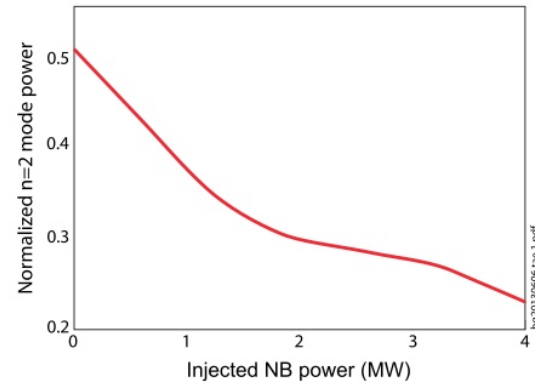


FIG. 12. Positive effect of the deposited NB power on the thermal plasma energy decay time. Also shown for comparison are numerical simulation results.

FIG. 13. Reduction in the mode power of the $n = 2$ rotational mode as a function of injected neutral beam power.

improvement in the plasma thermal energy decay time with increased deposited NB power. This is consistent with transport simulations produced with TAE's Q1D code, also shown in the figure.⁴⁵ Fast ions have a stabilizing effect on the rotational $n = 2$ instability in C-2. Figure 13 depicts the effective decrease in the mode power (proportional to the square of the mode amplitude) versus injected beam power. Indeed, due to high beam power in conjunction with edge rotation control, as discussed later, C-2 is stable against rotational modes. As a final example, Figure 14 shows electron heating during recent HPF14 discharges with about 2.5 MW of NB power absorbed. Based on Thomson scattering data, the electron temperature rises by $\sim 50\%$ in the edge between about 0.5 and 1 ms, with a lesser but notable rise in the core. Preferential edge heating is consistent with the fact that beam ions spend a large fraction of their orbits outside the separatrix. The later loss of heating is consistent with the radial and axial shrinkage of the FRC and withdrawal from the NB path. This corroborates with the resulting increase in NB shine through.

E. Stability

Most non-beam-driven FRCs show remarkable gross stability and surprising survivability even to large perturbations, such as high-speed translation and abrupt stopping of

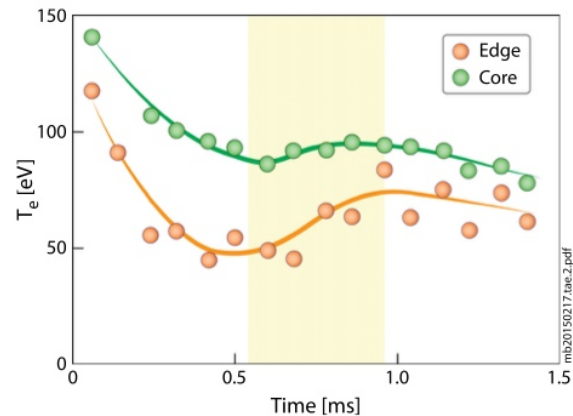


FIG. 14. Core and edge electron temperature from Thomson scattering.

056110-8 Binderbauer *et al.*

Phys. Plasmas 22, 056110 (2015)

the plasma. Historically, efforts to understand FRC stability have focused on three global modes, as outlined in Table II. The largest effort has addressed the tilt mode, which is unstable and rapidly disruptive according to ideal-MHD theory,⁴⁶ whereas in experiments the tilt, as a disruptive event, proved elusive. This apparent discrepancy fostered a protracted theory and simulation effort to explain the resilience. Rotational modes, on the other hand, were ubiquitous, although with a lower growth rate; they generally caused disruption of the FRC midway through its normal decay. Of the rotation-driven modes, the wobble, which radially shifts the FRC axis, and the $n = 2$ rotational mode (n is the toroidal mode number), an elliptical distortion of the plasma cross-section, are unmistakable in typical experiments. Higher-order rotational modes are usually weaker, probably because of stabilizing finite-Larmor-radius (FLR) effects. The wobble typically saturates at finite amplitude. The $n = 2$ mode has a higher growth rate and lower rotation threshold than the wobble and most often disrupts the FRC. It is, therefore, historically, the most concerning, but was experimentally suppressed by applying a quadrupole magnetic field.⁴⁷

Stability against $n = 2$ modes remains a concern for beam-driven FRCs, such as C-2. Many studies have explored the effects of large-orbit ions and predicted stabilizing influences from their highly kinetic nature, and the stiffening effect arising from their large angular momentum.^{1,2,6} Nonetheless, C-2 was designed to include stabilizing quadrupole fields, provided by a set of saddle coils, wound directly onto the central confinement vessel. In non-HPF operation, and without an appreciable fast-ion pressure, the $n = 2$ mode is clearly observed and ultimately compromises the discharge.^{3,14} Applying a quadrupole field (with strength at the separatrix $\sim 10\%$ of the external field) significantly delays the onset of the $n = 2$ mode, but cannot completely suppress it since the quadrupole field at the separatrix weakens as the plasma radius shrinks. Figure 15 shows the temporal evolution of a typical non-HPF discharge without fast-ion pressure, but with applied quadrupoles. In this example, the onset of the $n = 2$ mode is delayed until ~ 0.7 ms. It then appears as a large modulation in the line-integrated density signal, $\int n_e d\ell$, and is also seen by tomography as an elliptical distortion of the FRC cross section, rotating in the ion diamagnetic direction. Significant $n = 2$ activity is noticeable around 0.7–0.8 ms, leading to rapid loss of confinement.

While quadrupole stabilization can prevent or delay the elliptical deformation, it has negative attributes: (1) the quadrupole field significantly distorts the field lines near and outside the separatrix, bending them so that they intercept

TABLE II. FRC macro-instabilities of greatest concern.

n (toroidal)	m (poloidal)	Mode name	Found in FRCs?	Limits C-2 HPF?
Rotating				
2	1	$n = 2$	Yes	No
1	1	Wobble	Yes	No
Non-rotating				
≥ 1	1	Tilt	Yes	No

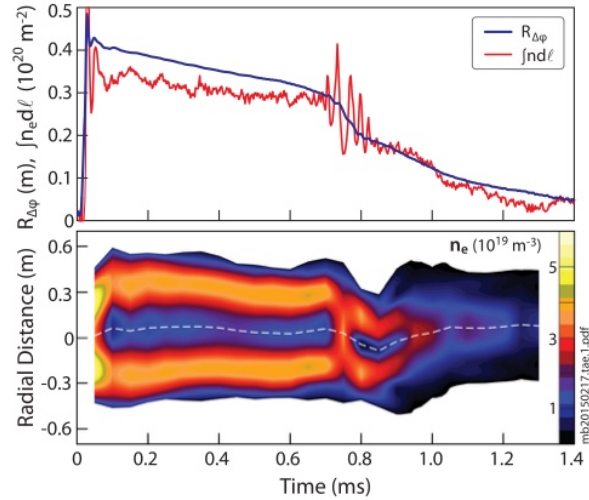
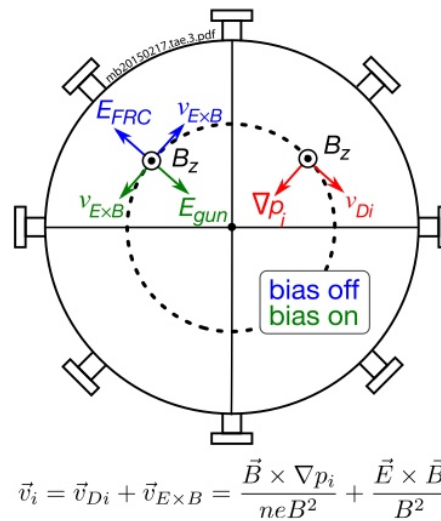


FIG. 15. Rotational instability in typical non-HPF discharge without fast particle pressure. Shown in the upper frame is the temporal evolution of the excluded flux radius, $R_{\Delta\Phi}$, and the line integrated density $\int n_e d\ell$ at the $r = 3.3$ cm radial chord of a six-channel integrated CO₂/HeNe interferometer system at the C-2 midplane. The lower frame shows contours of the electron density, n_e , found by Abel inversion of the interferometer measurements.

nearby side walls, resulting in partial wall contact and lower temperatures, and (2) since the quadrupole field breaks azimuthal symmetry, the canonical angular momentum is no longer conserved, which compromises plasma confinement and leads to rapid pump out of fast ions via stochastic diffusion to the walls.⁴⁸ Suppressing $n = 2$ modes is, therefore, of paramount importance in an NB-driven system. A low- n asymmetry, whether quadrupole-generated or instability generated, is unacceptable.

This challenge was resolved by biasing field surfaces in the SOL so as to create a radially inward electric field in the SOL, producing an $E \times B$ drift that counteracts the FRC's natural diamagnetic rotation and spin up. Figure 16 illustrates the mechanism. The azimuthal ion flow is the sum of the



$$\vec{v}_i = \vec{v}_{Di} + \vec{v}_{E \times B} = \frac{\vec{B} \times \nabla p_i}{neB^2} + \frac{\vec{E} \times \vec{B}}{B^2}$$

FIG. 16. Contributions to ion rotational velocity.

056110-9 Binderbauer et al.

Phys. Plasmas 22, 056110 (2015)

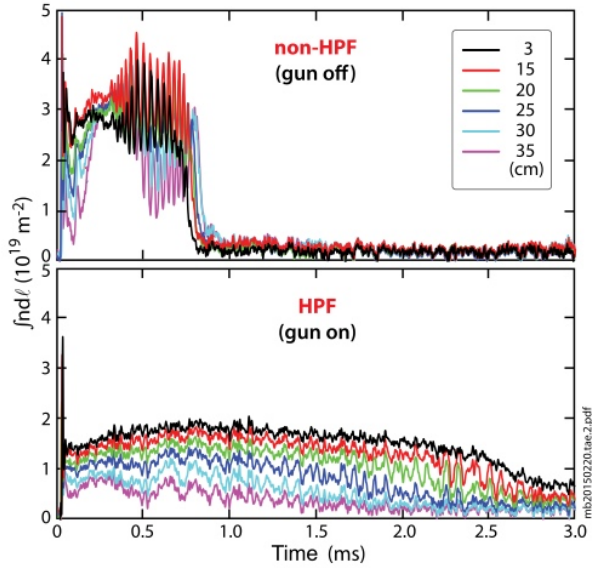


FIG. 17. Line integrated density of two C-2 discharges, the upper frame without divertor biasing (gun off) and the lower frame with (gun on).

diamagnetic and $E \times B$ drifts, $\mathbf{v}_i = (\mathbf{B} \times \nabla p_i)/n_e e B^2 + (\mathbf{E} \times \mathbf{B})/B^2$, where \mathbf{B} and \mathbf{E} are the local magnetic and electric fields, e is the electron charge, and p_i is the ion plasma pressure. In typical FRCs, the edge electric field points outward so that the two drift-terms are additive, causing spin-up. Proper biasing via the plasma-gun electrodes can reverse the electric field, which opposes spin-up. Thus, this technique suppresses the effect (rotation) that drives the rotational instability, and *without* breaking symmetry, thereby avoiding any negative impact on fast-ion confinement. As such it is a critical element enabling stable HPF discharges in C-2. Figure 17 shows examples of line-integrated density $\int n_e d\ell$ traces for non-HPF (top panel) and HPF (lower panel) discharges. With gun off, (top panel), an $n=2$ disturbance emerges at ~ 0.3 ms, leading to disruption of the FRC at ~ 0.8 ms. In contrast, with gun on (lower panel), no $n=2$ signature appears during the first roughly 3 ms. The oscillations appearing earlier are due to a modest, low-frequency wobble mode. Combining edge biasing and higher-power NB injection renders HPF discharges essentially stable

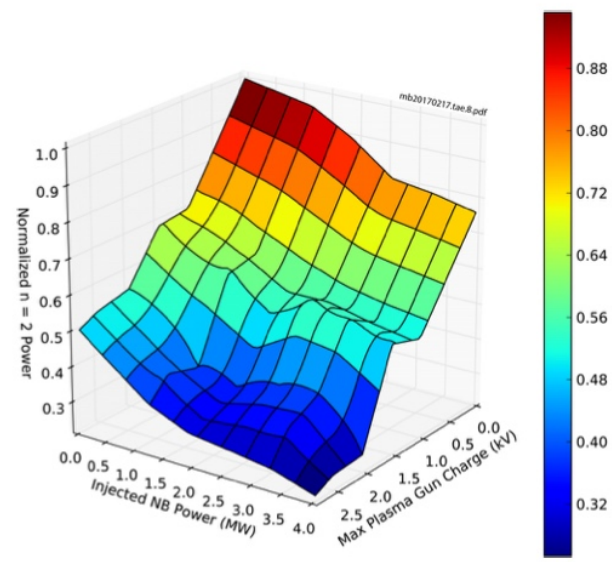


FIG. 18. Normalized $n=2$ power (proportional to the square of the mode amplitude) as a function of injected NB power and bias potential on the plasma gun electrodes. The plot is derived from a large ensemble of HPF discharges, only varying the two indicated parameters.

to $n=2$ modes. Figure 18 illustrates the effectiveness of the combined technique, showing that the lowest $n=2$ mode power occurs when the two methods are combined.

The wobble mode is of much lesser concern, as it typically saturates at lower amplitudes and rarely causes disruption of the FRC. It manifests itself as an off-axis displacement of the FRC centroid, as readily observable from, e.g., bolometry data. Line-tying between the FRC plasma and conducting end surfaces (e.g., gun electrodes) can stabilize wobble motion, with the tension of the magnetic field lines acting as the restoring force. Stability, therefore, requires sufficient plasma density ($\sim 10^{12} \text{ cm}^{-3}$) in front of the guns, as line-tying is limited by sheath resistance. Operating plasma guns at both ends and biasing the magnetic field lines to about -400 V reduce wobble in C-2 HPF discharges to negligible levels, as illustrated in Figure 19. The left panel, a case without divertor biasing, exhibits a wobble motion with large radial displacement. The right panel with

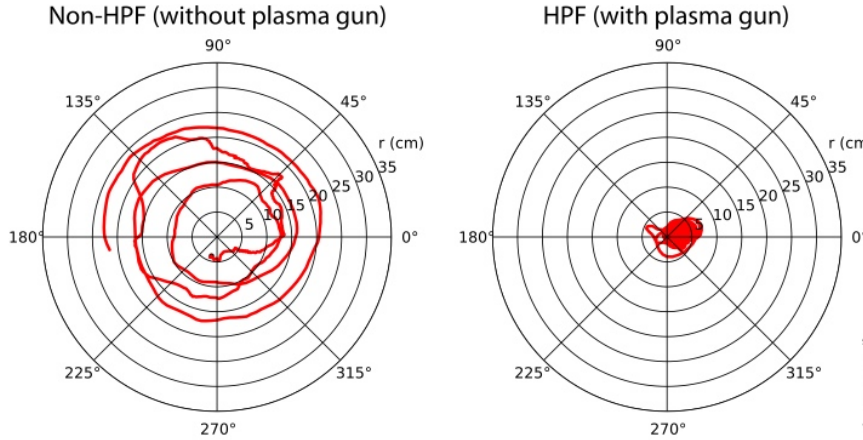


FIG. 19. Trajectories of the FRC centroid motion as a function of time as determined from bolometer based tomography.

056110-10 Binderbauer *et al.*

Phys. Plasmas 22, 056110 (2015)

biasing shows minuscule wobble. The resultant strong centering provides for more efficient coupling of the neutral beams to the FRC plasma. This is especially critical during the early discharge (> 1 ms) to maximize the build-up of fast particle pressure.

The potential for tilting is inherent in the FRC topology, as it represents an anti-aligned magnetic dipole embedded in an opposing exterior field. The plasma currents generate the pressure that drives the instability. Theoretical analyses of an ideal tilt point to an extremely short growth time on an Alfvénic time scale of a few microseconds. These predict that the tilt distorts the internal field structure with very little disturbance outside the separatrix, which makes it very difficult to diagnose directly. Tilt detection must, therefore, rely on indirect inferences. The tilt growth rate is known to be reduced by elongation of the separatrix. However, actual stability must rely on other effects, particularly large-orbit ions as a result of: (1) ion skin depth effects, (2) gyroviscous stress from magnetized ions, and (3) betatron-orbit phase-averaging, making the fast-ion population largely immune to the disturbance. Theoretically, there is a tilt stability threshold that places an upper bound on S^*/E , where $S^* = R_s/(c/\omega_{pi})$ is the radial size parameter (c/ω_{pi} is the ion skin depth, $\omega_{pi}^2 = 4\pi n_e e^2/m_i$) and $E = Z_s/R_s$ is the separatrix elongation. The empirical stability threshold is about $S^*/E < 3-3.5$ based on many observations of long-lived FRCs. This value is roughly consistent with the theoretical stability bound. C-2 HPF discharges are typically operated in the stable regime mainly by controlling density. Introducing a significant fast-ion pressure also helps. Nonetheless, indirect evidence of tilting can be observed in C-2 under deliberately adverse conditions.

To illustrate the difference in behavior, Fig. 20 contrasts a series of discharges that exhibit a partial- or totally disruptive event strongly consistent with tilting (thin lines) with an example of stable and totally quiescent operation (thick trace). The features that appear are as follows. (1) The events are preceded by a rapid buildup in midplane density (second panel from top). (2) Radiative emissions rise rapidly with a slight time delay at a location axially offset from the midplane and at the end of the FRC (second panel from bottom). (3) The event is followed by a rapid axial lengthening of the FRC (bottom panel). Figure 21 makes a connection between these events and the evolution of S^*/E . The time progression is from right to left. The stable discharge (solid squares) stays well below the nominal stability boundary at $S^*/E = 3$, while the two unstable shots (solid and open circles and triangles) closely approach or cross the boundary and “bounce” away. In one case (#24014), the event partially releases the stored free energy and “resets” the discharge away from the stability boundary, while in another (#24049) it causes a much more severe change.

Finally, a comment is in order on possible fast-ion-driven modes and effects in C-2. To date, there is no evidence of destructive modes induced by the pronounced fast-ion population. Indeed, the macroscopic modes discussed here all benefit from the stabilizing influence of the

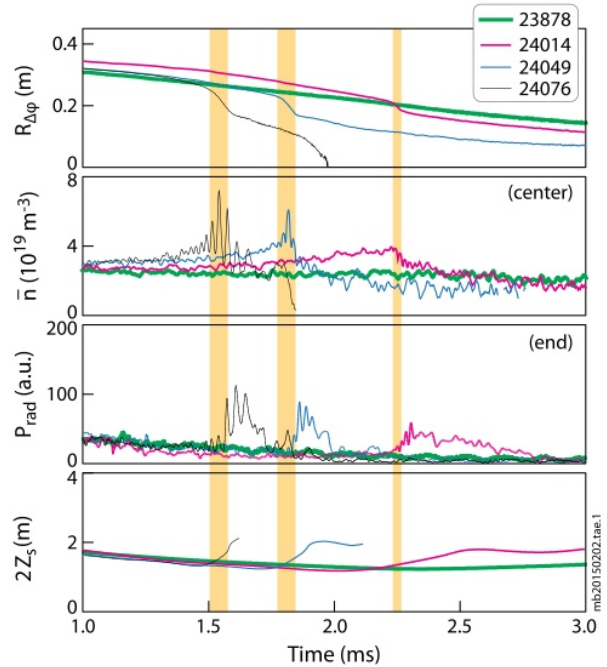


FIG. 20. Time traces of a selection of discharges featuring stable (thick trace) or tilt (light traces) activity. Shown are the excluded flux radius (top panel), line averaged electron density at midplane (second from top), radiated power at $z = -1$ m from the midplane (second from bottom), and separatrix length (bottom panel). Yellow vertical lines indicate the time when tilting is likely active in the unstable discharges.

fast ions. It is also worth noting that the ratio of fast-ion energy to plasma temperature is larger in C-2 than it will be in contemplated future higher energy facilities. The fast-ion pressure is also comparable to the plasma pressure in the C-2 HPF regime. However, the non-observance of destructive modes, while important, is not proof that fast-ion induced activity does not occur. In fact, there is both theoretical and experimental evidence of fast-ion-related magnetic fluctuations in C-2.⁴⁴ Experimentally, in HPF deuterium discharges,

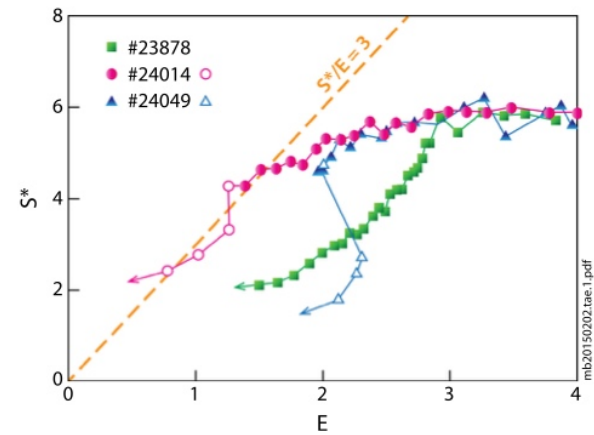


FIG. 21. Evolution of S^*/E parameters for stable (solid squares) and unstable (circles and triangles) discharges. Also shown is the nominal tilt stability boundary at $S^*/E = 3$. Open symbols indicate the further progression of the discharge after onset of instability.

056110-11 Binderbauer *et al.*

Phys. Plasmas 22, 056110 (2015)

these fluctuations appear in the azimuthal magnetic field, B_θ , near the fast ion orbit frequency, and scale linearly with magnetic field. Higher NB power decreases the broadband magnetic fluctuations and also appears to reduce the peak fluctuation amplitude. In C-2 simulations, the fluctuations primarily appear in the radial magnetic field, B_r , at about twice the fast ion axial bounce frequency. These fluctuations redistribute fast ions away from the axial turning points.

F. Confinement

The pristine environment of C-2 with its macroscopically stable, well-centered, and relatively quiescent discharges has enabled imaging of broadband density turbulence in detail for the first time in an FRC (in the core and SOL). Measurements in previous FRCs have been largely restricted to coherent mode magnetic fluctuations,⁴⁹ high frequency modes (in particular, lower hybrid drift instabilities⁵⁰), or probe measurements near the FRC boundary or separatrix. In contrast, DBS measurements allow non-perturbing measurements of the FRC core and edge plasma, and determination of the toroidal turbulence wavenumber spectrum. The plasma-frame frequency spectrum of modes investigated here peaks below 100 kHz (below the ion cyclotron frequency), however, the detected DBS spectrum is dominated by the Doppler shift as a result of toroidal $E \times B$ plasma rotation, as described in more detail in Ref. 38. The DBS diagnostics is complemented by FIR laser forward scattering as described in Ref. 37.

As a direct result, various critical confinement properties of C-2 plasmas are clearly emerging. Figure 22 shows the relative density fluctuation profile from the DBS system. The radius coordinate is referenced to the excluded-flux radius location, which is roughly the same as the separatrix radius so that negative values are in the core and positive in the SOL. The core is quiescent, and the fluctuations rise significantly in the SOL. Figure 23 shows the density fluctuations from the FIR system. These results correlate with the picture emerging from DBS, namely, relatively quiescent behavior in the core with peaking fluctuations in the SOL. Evidently,

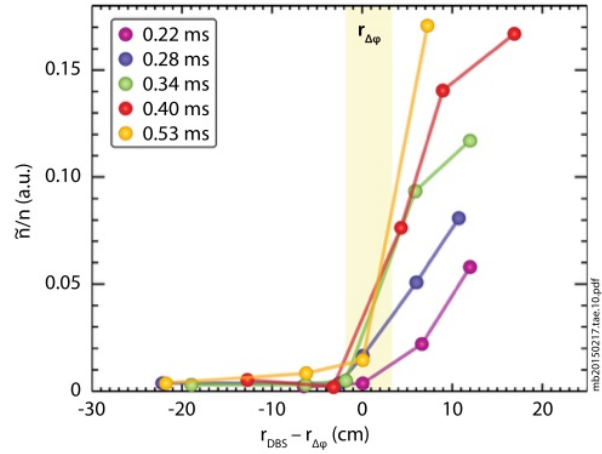


FIG. 22. Relative density fluctuations as a function of radial position as measured by the microwave Doppler backscattering (DBS) diagnostic.

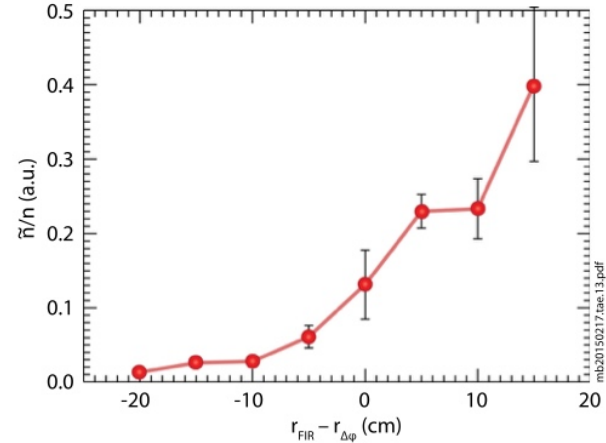


FIG. 23. Relative density fluctuations as a function of radial position as imaged by the far-infrared (FIR) forward scattering diagnostic.

the absolute fluctuation levels peak in the locals where the density and temperature gradients are steepest, namely, at or just outside the separatrix. While the relative fluctuation amplitudes increase with radius in the SOL. Most importantly, C-2 HPF plasmas exhibit very low fluctuation levels in the core.

Comparing the nature of fluctuations in the non-HPF and HPF regimes, certain features stand out. In the non-HPF case (e.g., plasma gun off), a high level of fluctuations appear throughout the discharge as seen in the top panel of Fig. 24, while in the HPF regime (e.g., plasma gun on), the fluctuation level is several times lower (see Fig. 24, lower frame). Evidently, HPF operation dramatically reduces

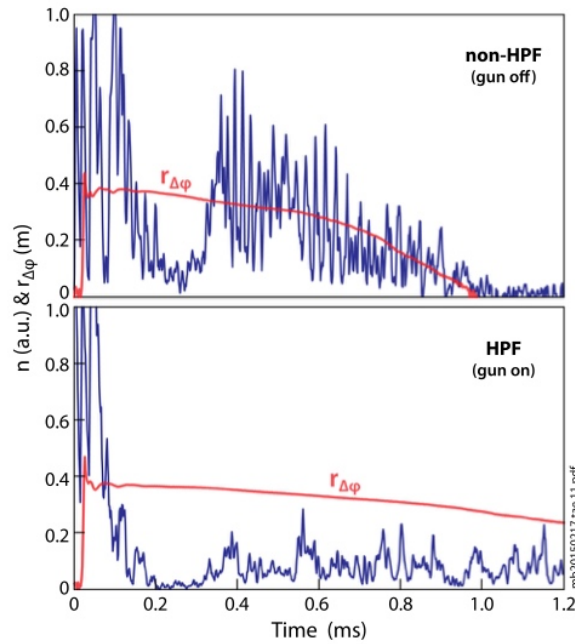


FIG. 24. Comparison of fluctuation levels, imaged by DBS, in non-HPF and HPF discharges as a function of time. Superimposed is a time trace of the excluded flux radius for each discharge.

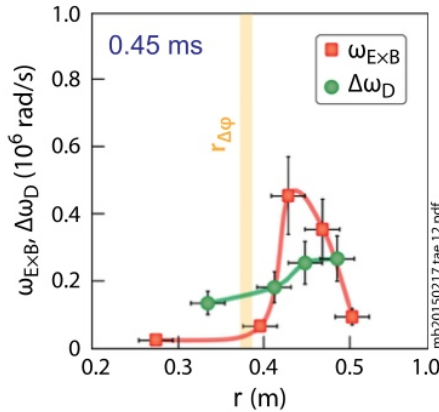


FIG. 25. Comparison of the $E \times B$ shearing rate, ω_{ExB} , and the turbulence decorrelation rate, $\Delta\omega_D$, at about $450 \mu s$ into the discharge. The $E \times B$ shearing rate is calculated from the difference in $E \times B$ velocity between neighboring radial DBS measurement positions.

fluctuation. Further, the measured $E \times B$ flow has little shear in “non HPF,” while it has a large pronounced shear in HPF, as shown in Fig. 25. This is evidenced by the $E \times B$ shearing rate ω_{ExB} exceeding the turbulence decorrelation rate $\Delta\omega_D$ near and outbound of the separatrix. Clearly then, one of the key demarcations between non-HPF and HPF regimes is the presence of shear flows, which also correlates with the suppression of fluctuations. These trends are reminiscent of the L to H-mode transition in tokamaks.⁵¹

Figure 26 shows wavenumber spectra of the observed fluctuations. Outside the separatrix ($R_s + 5$ cm) is an exponentially falling spectrum with ion gyro-scale turbulence (Fig. 26, right panel). Here, k_θ is the azimuthal wavenumber and ρ_s is the ion sound gyroradius. Inside of the separatrix (core, $R_s - 5$ to 8 cm), the fluctuations are depressed by an order of magnitude at $k_\theta\rho_s < 10$ (Fig. 26, left panel). This highlights the importance of large orbits and shear effects in reducing fluctuations. On the other hand, the core spectrum

broadly peaks in the wavenumber range $k_\theta\rho_s \sim 15-45$ with the core fluctuations out to $k_\theta\rho_e \sim 0.3$ (ρ_e is the electron gyroradius), i.e., the core fluctuations suggest the presence of electron modes. As conjectured in the 1990s by Rostoker and Binderbauer,⁶ a population of large-orbit ions, especially in NB-driven FRCs, can average out short-wavelength fluctuations and as such substantially stabilize both macroscopic and microscopic modes. Because of the latter, this effect also suppresses transport driven by microscale modes. On the other hand, modes on the pronounced sub-ion gyroradius scale (higher $k_\theta\rho_s$) as observed presently are not strongly influenced by large-orbit ions. For C-2 parameters, electron-temperature-gradient modes are not prominently unstable as $\eta_e = L_N/L_{Te} \sim 1$, where L_N and L_{Te} are the density and electron temperature gradient lengths, respectively. The nature of these electron modes is currently under active investigation.⁵²

In view of these fluctuation measurements, one expects that improved global confinement of particles and energy might accrue in the reduced-fluctuation HPF environment. In C-2 FRCs, where even the thermal-ion gyroradius is significant, ions tend to behave near classically, while the electron physics drives anomalous transport. Figure 27 plots the electron energy confinement time, τ_{Ee} , versus electron temperature for two ensembles of C-2 HPF conditions (HPF12 and HPF14). The most notable feature of these observations is the strongly favorable T_e scaling of the confinement time. Current best fits of C-2 data show $\tau_{Ee} \propto T_e^{1.6}$. This scaling is in stark contrast to the well-known Bohm scaling which has $\tau_{Ee} \sim T_e^{-1}$. Such scaling differences have also been observed in recent experiments in spherical (high-beta) tokamaks.⁵³

In parallel to improvements in energy confinement, HPF plasmas in C-2 also exhibit dramatic improvements in particle confinement when compared to past FRC experiments. Figure 28 compares the particle confinement time τ_N for various C-2 configurations and many other past and present FRC experiments, as plotted against the standard theta-pinch

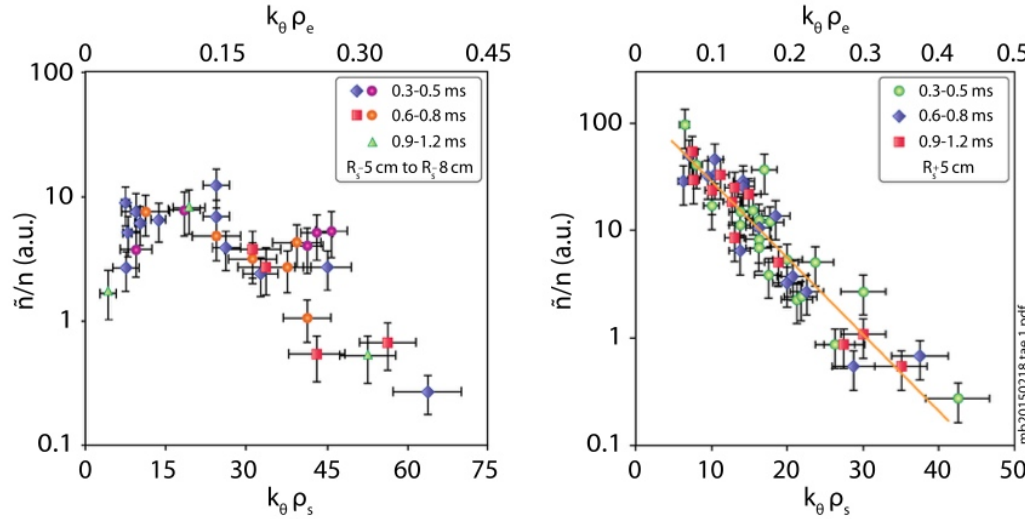


FIG. 26. DBS based wavenumber spectra inside and outside of the core. While DBS does not allow absolute density fluctuation measurements, the arbitrary scales utilized in the left and right panels are identical.

056110-13 Binderbauer et al.

Phys. Plasmas 22, 056110 (2015)

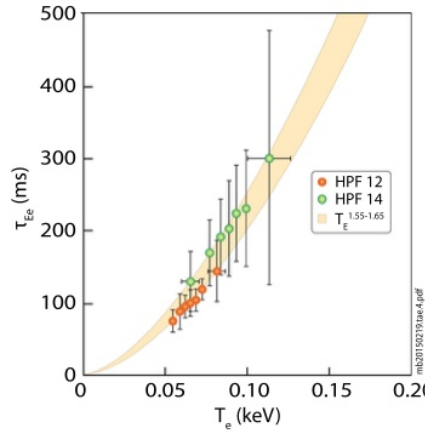


FIG. 27. Global energy confinement time of electrons as a function of temperature for ensembles of HPF12 and HPF14 discharges.

FRC scaling, $\tau_N \propto R_s^2 n_e^{1/2}$. Clearly, the HPF particle confinement time in C-2 is dramatically higher than conventional FRCs. Moreover, it departs completely from the standard scaling law with optimized C-2 conditions exhibiting a tenfold improvement in particle confinement at similar plasma size. It is important to note that the current C-2 plasma is already quite collisionless: the ion mean-free-path is far greater than the FRC dimensions such as R_s , and the electron mean-free-path is also longer. This lends support to the notion that the currently observed transport may be generically similar to that in the regime of projected future reactors. It is, thus, critical to ascertain on how this will manifest in a future facility that extends plasma parameters much beyond C-2, and further into the collisionless regime.

A further topic of interest is the nature of the relationship between FRC core and SOL confinement. One notes that

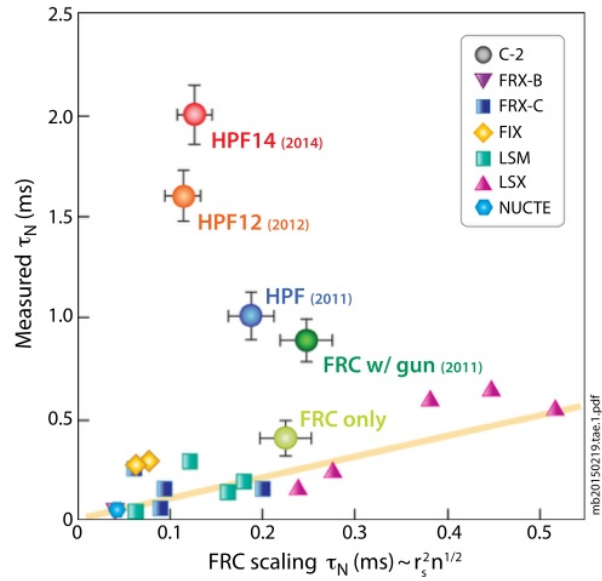


FIG. 28. Global particle confinement time in the evolving C-2 experiments as compared with other FRC experiments. Each data point represents averages derived from an ensemble of similar discharges.

particle and energy transport times across these regions are sequential, i.e., it takes a composite time for particles and energy to get lost from the core to the outside of the FRC system by both experiencing the transport processes in the core and then in the SOL. On the other hand, the respective confinement times themselves are also coupled with each other. An illustrative example of this interdependence is provided by studies in C-2 where the SOL conditions are changed by modifying the magnetic field strengths of the formation, B_{FS} , and mirror plugs, B_{plug} . As illustrated in Figure 29, increasing both B_{FS} and B_{plug} considerably improves the global electron energy confinement time, τ_{ee} . Furthermore, the increase in B_{FS} is a prerequisite for the increase in B_{plug} to have a favorable effect on confinement. Minimizing the SOL end loss rate calls for higher B_{FS} to prevent substantial wall contact in the formation tubes and to enable the possibility of particles being “bounced back” by the mirror plugs. Moreover, improving the end confinement time in the SOL broadens the SOL and reduces its gradients. This in turn reduces the edge fluctuations and thus reduces the transport rate out of the core (edge-gradient dependence of the core). In terms of global performance, the most recent HPF experiments (HPF14) clearly demonstrate the positive ramifications of the core-SOL coupling, as seen in Figures 1, 2, 27, 28, and 29, which collectively illustrate the correlation between FRC lifetime and the SOL control knobs discussed here.

Overall, critical transport findings in C-2 can be summarized as follows:

- (1) The fast-ion confinement appears to be classical.
- (2) In the core, the fluctuation level is quite low and the plasma relatively quiescent. This leads to the inverted wavenumber spectrum of fluctuations in the core, showing evidence of FLR effects and/or $E \times B$ shear stabilization of longer wavelength ion modes, consistent with the observed near-classical core thermal ion transport. The evidence suggests electron-scale modes, which may be the cause of the anomalous electron thermal transport at up to 20 times classical. The overall electron energy transport τ_{ee} shows a positive power dependence on the electron temperature, in sharp contrast to most other anomalous electron transport observations or theories.

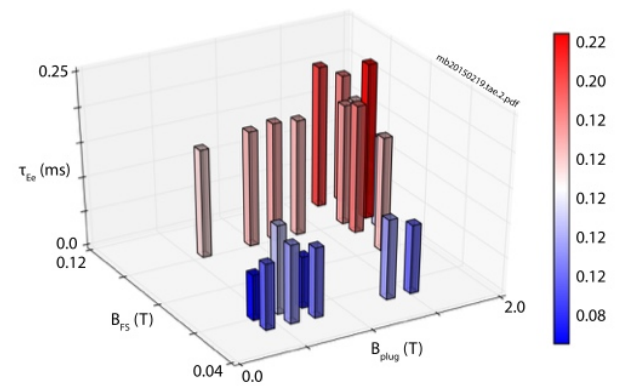


FIG. 29. Dependence of the global electron energy confinement time, τ_{ee} , on the strength of the formation, B_{FS} , and mirror plug, B_{plug} , magnetic fields.

056110-14 Binderbauer *et al.*

Phys. Plasmas 22, 056110 (2015)

- (3) In the edge, fluctuations peak in the SOL region near the separatrix. The fluctuation spectrum shows exponentially falling ion gyro-scale turbulence up to $k_\theta \rho_s < 50$. There is tentative evidence of a critical density gradient, controlling the onset of density fluctuations.⁵⁴ If so, the density gradients adjust self-consistently toward the critical value.⁵⁵
- (4) Furthermore, the transport phenomena in the core and in the SOL are close-coupled. Control-knobs have been employed that affect the SOL transport, which in turn influences the core transport. The SOL turbulence can affect the overall FRC lifetime and confinement.
- (5) There may be a thermal barrier near the separatrix, a topic under active investigation.

III. NEXT STEPS

Given the success with and insights gained by operating C-2, which was designed to study the limiting physics of stability and transport, TAE is now installing a major upgrade, C-2U. This is motivated by two main considerations: (1) After breakthrough confinement and stable operation in the C-2 HPF regime, the next most interesting physics question is whether neutral beam based current drive is feasible in beam-driven FRCs. (2) The beam-plasma coupling efficiency in C-2 is primarily limited by the shrinking FRC size, fast ion energy relative to magnetic field, as well as physical location and aim of NB injectors. The key improvements in C-2U are specifically directed towards addressing these concerns via a major upgrade to the NB system as well as the location and orientation of individual injectors. The ultimate goal of C-2U is to demonstrate FRC sustainment via NBI and refueling. This means that key plasma parameters such as thermal energy, particle inventory, and trapped flux will need to be maintained at appropriate levels throughout the discharge, with substantial decay only evident post NB termination. To make a strong case, this further requires the sustained FRC lifetime to be on order of or longer than the characteristic times scales associated with confinement ($\tau_E \leq 0.8$ ms, $\tau_N \leq 2$ ms), fast ion slowing down ($\tau_s \leq 3$ ms), and current decay ($\tau_{L/R} \leq 3$ ms). Based on C-2 data and the fact that C-2U will operate at similar plasma performance, a “flat” phase of 5+ ms in C-2U should be sufficient.

Present results clearly point to the need for more power to sustain the configuration. In C-2, the plasma loses an aggregate of about 3.5–4 MW about midway through the discharge. Even under perfect conditions, the present NB system cannot maintain the plasma energy vis-à-vis these losses. This prompts an upgrade in overall beam power from about 4 MW in C-2 to 10 MW in C-2U. To further increase the coupling of injected fast ions to the core, the energy of the C-2U beams will be reduced from 20 keV to 15 keV at close to triple the equivalent neutral current.

Moreover, because of the energy, particle, and flux losses, the FRC is shrinking throughout the discharge, with the rate of axial contraction outpacing the radial decrease. This presents a major coupling challenge. In C-2, most NB injectors are distributed along the machine axis; with the consequence that total shine-through increases considerably

when outer neutral beams begin to miss the shrinking core plasma. To safeguard against that, C-2U will locate all beams very close to the machine center and also aim the beams at a 15°–25° angle (adjustable per C-2U campaign objectives) relative to the machine mid-plane. A basic layout is indicated in Figure 30. This angled tangential injection will further reduce the radial scale of the fast ion orbits and provide better coupling to the core. In addition, the beams new axial kinetic energy will cause considerable axial spread of fast ions and increase the turning point pressure near the FRC ends, further counteracting shrinkage. Based on extensive C-2U simulations, calibrated on C-2 data, the more central locations and angled NBI, combined with lower ion energy and higher current, will dramatically increase the coupled power throughout the discharge and help to sustain the FRC. Based on the same simulations, particle inventory control will require auxiliary fueling via pellets and/or compact torus injection,⁵⁶ both of which have been tested and validated in C-2.

IV. SUMMARY

Over the past 5+ years, the C-2 program has demonstrated effective FRC formation via collisional merging, long lifetime FRC discharges, stability control and fluctuation suppression from the edge, and the dramatic beneficial impact of fast ions on overall plasma performance. The considerably abstracted and fully automated machine operation testifies to the mature engineering integration of the many highly complex subsystems. Most importantly, careful performance optimization led to the discovery of the HPF regime, which is characterized by (1) macroscopically stable discharges (lifetime only limited by transport), (2) excellent shot-to-shot reproducibility, (3) dramatically reduced transport rates (up to an order of magnitude improvement compared to non-HPF regime), (4) minimized radiative losses, (5) record diamagnetism lifetimes (exceeding 5 ms), (6)

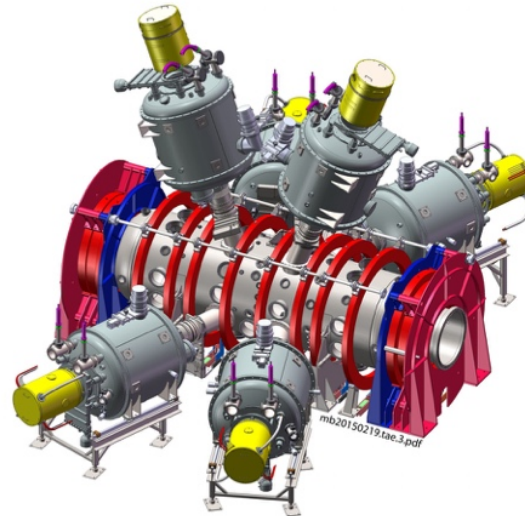


FIG. 30. CAD based rendering of the revised central section of C-2U, showing location and aim of the upgraded neutral beam injectors.

056110-15 Binderbauer *et al.*Phys. Plasmas **22**, 056110 (2015)

coupled FRC core-to-SOL transport paradigm (a double transport barrier, intercoupling core, and SOL physics), and (7) emerging global energy confinement scaling with strong positive temperature dependence. Together these achievements anticipate sustainment techniques to be exploited and further enhanced in future TAE facilities. In fact, heating, current drive, and overall sustainment appear to be within reach of a selective C-2 upgrade, C-2U, with operation starting in early 2015. Collectively, these accomplishments represent a dramatic advance towards the FRC relevant scientific goal of “demonstrating that a compact toroid with simply connected vessel can achieve a stable, long-pulsed plasma at kilovolt temperatures with favorable confinement scaling to proceed to a pre-burn CT plasma experiment.”

ACKNOWLEDGMENTS

We thank our shareholders for their support and trust, and all fellow TAE staff for their dedication, excellent work, and extra efforts. We are also indebted to the many members of the Budker Institute for their excellent technical contributions and superb on-site assistance. Above all, we are grateful for the scientific genius and remarkable intuition of Norman Rostoker. Sadly Norman passed away during the revision of this manuscript in late December 2014. While a co-author of this publication, the rest of the authors would like to dedicate this work to Norman. He was a singular visionary and this program and Tri Alpha Energy would not exist without his groundbreaking efforts, courage, and perseverance.

¹M. Tuszeowski, *Nucl. Fusion* **28**, 2033 (1988).

²L. C. Steinhauer, *Phys. Plasmas* **18**, 070501 (2011).

³M. W. Binderbauer, H. Y. Guo, M. Tuszeowski, S. Putvinski, L. Sevier, D. C. Barnes, N. Rostoker, M. G. Anderson, R. Andow, L. Bonelli, F. Brandi, R. Brown, D. Q. Bui, V. Bystritskii, F. Ceccherini, R. Clary, A. H. Cheung, K. D. Conroy, B. Deng, S. A. Detrick, J. D. Douglass, P. Feng, L. Galeotti, E. Garate, F. Giannanco, F. J. Glass, O. Gornostaeva, H. Gota, D. Gupta, S. Gupta, J. S. Kinley, K. Knapp, S. Korepanov, M. Hollins, I. Isakov, V. A. Jose, X. L. Li, Y. Luo, P. Marsili, R. Mendoza, M. Meekins, Y. Mok, A. Necas, E. Paganini, F. Pegoraro, R. Pousa-Hijos, S. Primavera, E. Ruskov, A. Qerushi, L. Schmitz, J. H. Schroeder, A. Sibley, A. Smirnov, Y. Song, L. C. Steinhauer, X. Sun, M. C. Thompson, A. D. Van Drie, J. K. Walters, and M. D. Wyman, *Phys. Rev. Lett.* **105**, 045003 (2010).

⁴N. Rostoker, F. J. Wessel, H. U. Rahman, B. C. Maglich, B. B. Spivey, and A. Fisher, *Phys. Rev. Lett.* **70**, 1818 (1993).

⁵N. Rostoker and M. Binderbauer, *Bull. Am. Phys. Soc.* **38**, 1976 (1993).

⁶M. Binderbauer and N. Rostoker, *J. Plasma Phys.* **56**, 451 (1996).

⁷D. C. Barnes, J. L. Schwarzmeyer, H. R. Lewis, and C. E. Seyler, *Phys. Fluids* **29**, 2616 (1986).

⁸H. Naitou, T. Kamimura, and J. Dawson, *J. Phys. Soc. Jpn.* **46**, 258 (1979).

⁹R. Horiuchi and T. Sato, *Phys. Fluids B* **1**, 581 (1989).

¹⁰W. W. Heidbrink and G. J. Sadler, *Nucl. Fusion* **34**, 535 (1994).

¹¹R. Hazeltine, “Research Needs for Magnetic Fusion Energy Sciences Report of the Research Needs Workshop (ReNeW),” U.S. Department of Energy, Washington DC, 2009, pp. 171–227.

¹²D. N. Hill, “Report of the FESAC Toroidal Alternates Panel,” U.S. Department of Energy, Washington DC, 2008.

¹³X. Yang, H. Gota, M. Binderbauer, M. Tuszeowski, H. Guo, E. Garate, D. Barnes, S. Putvinski, T. Tajima, and L. Sevier, *Bull. Am. Phys. Soc.* **59**, UP8.00002 (2014).

¹⁴H. Y. Guo, M. W. Binderbauer, D. Barnes, S. Putvinski, N. Rostoker, L. Sevier, M. Tuszeowski, M. G. Anderson, R. Andow, L. Bonelli, F. Brandi, R. Brown, D. Q. Bui, V. Bystritskii, F. Ceccherini, R. Clary, A. H. Cheung, K. D. Conroy, B. H. Deng, S. A. Detrick, J. D. Douglass, P. Feng, L. Galeotti, E. Garate, F. Giannanco, F. J. Glass, O. Gornostaeva,

H. Gota, D. Gupta, S. Gupta, J. S. Kinley, K. Knapp, S. Korepanov, M. Hollins, I. Isakov, V. A. Jose, X. L. Li, Y. Luo, P. Marsili, R. Mendoza, M. Meekins, Y. Mok, A. Necas, E. Paganini, F. Pegoraro, R. Pousa-Hijos, S. Primavera, E. Ruskov, A. Qerushi, L. Schmitz, J. H. Schroeder, A. Sibley, A. Smirnov, Y. Song, L. C. Steinhauer, X. Sun, M. C. Thompson, A. D. Van Drie, J. K. Walters, and M. D. Wyman, *Phys. Plasmas* **18**, 056110 (2011).

¹⁵M. Tuszeowski, A. Smirnov, M. C. Thompson, S. Korepanov, T. Akhmetov, A. A. Ivanov, R. Voskoboinikov, L. Schmitz, D. Barnes, M. W. Binderbauer, R. Brown, D. Q. Bui, R. Clary, K. D. Conroy, B. H. Deng, S. A. Detrick, J. D. Douglass, E. Garate, F. J. Glass, H. Gota, H. Y. Guo, D. Gupta, S. Gupta, J. S. Kinley, K. Knapp, S. Korepanov, A. Longman, M. Hollins, X. L. Li, Y. Luo, R. Mendoza, Y. Mok, A. Necas, S. Primavera, E. Ruskov, J. H. Schroeder, L. Sevier, A. Sibley, Y. Song, X. Sun, E. Trask, A. D. Van Drie, J. K. Walters, and M. D. Wyman, *Phys. Rev. Lett.* **108**, 255008 (2012).

¹⁶M. Tuszeowski, A. Smirnov, M. C. Thompson, T. Akhmetov, A. A. Ivanov, R. Voskoboinikov, D. Barnes, M. W. Binderbauer, R. Brown, D. Q. Bui, R. Clary, K. D. Conroy, B. H. Deng, S. A. Detrick, J. D. Douglass, E. Garate, F. J. Glass, H. Gota, H. Y. Guo, D. Gupta, S. Gupta, J. S. Kinley, K. Knapp, S. Korepanov, A. Longman, M. Hollins, X. L. Li, Y. Luo, R. Mendoza, Y. Mok, A. Necas, S. Primavera, E. Ruskov, L. Schmitz, J. H. Schroeder, L. Sevier, A. Sibley, Y. Song, X. Sun, E. Trask, A. D. Van Drie, J. K. Walters, and M. D. Wyman, *Phys. Plasmas* **19**, 056108 (2012).

¹⁷G. I. Dimov, A. A. Ivanov, and G. V. Roslyakov, *Sov. J. Plasma Phys.* **8**, 546 (1982).

¹⁸T. D. Akhmetov, V. S. Belkin, I. O. Bespamyatnov, V. I. Davydenko, G. I. Dimov, Yu. V. Kovalenko, A. S. Krivenko, P. A. Potashov, V. V. Razorenov, V. B. Reva, V. Ya. Savkin, and G. I. Shulzhenko, *Trans. Fusion Sci. Technol.* **43**, 58 (2003).

¹⁹L. Galeotti, D. C. Barnes, F. Ceccherini, and F. Pegoraro, *Phys. Plasmas* **18**, 082509 (2011).

²⁰M. C. Thompson, B. H. Deng, J. D. Douglas, D. Gupta, J. S. Kinley, A. Necas, X. Sun, A. D. VanDrie, and M. D. Wyman, *Bull. Am. Phys. Soc.* **56**, CP9.00100 (2011).

²¹E. Garate, N. Bolte, D. K. Gupta, H. Gota, I. Allfrey, J. Kinley, and K. Knapp, *Bull. Am. Phys. Soc.* **59**, UP8.00009 (2014).

²²A. Sorokin, V. Belov, V. Davydenko, P. Deichuli, A. Ivanov, A. Podyminogin, I. Shikhovtsev, G. Shulzhenko, N. Stupishin, and M. Tiunov, *Rev. Sci. Instrum.* **81**, 02B108 (2010).

²³H. Gota, M. C. Thompson, M. Tuszeowski, and M. W. Binderbauer, *Rev. Sci. Instrum.* **85**, 11D836 (2014).

²⁴F. Glass, B. H. Deng, E. Garate, O. Gornostaeva, and J. Schroeder, *Rev. Sci. Instrum.* **81**, 10D506 (2010); K. Zhai, B. Deng, J. Kinley, and J. Schroeder, *Bull. Am. Phys. Soc.* **58**, GP8.00041 (2013).

²⁵O. Gornostaeva, B. H. Deng, E. Garate, H. Gota, J. Kinley, J. Schroeder, and M. Tuszeowski, *Rev. Sci. Instrum.* **81**, 10D516 (2010); B. H. Deng, J. S. Kinley, and J. Schroeder, *ibid.* **83**, 10E339 (2012).

²⁶F. Brandi and F. Giannanco, *Opt. Lett.* **32**, 2327 (2007); F. Brandi, F. Giannanco, W. S. Harris, T. Roche, E. Trask, and F. J. Wessel, *Rev. Sci. Instrum.* **80**, 113501 (2009).

²⁷M. C. Thompson, J. D. Douglass, P. Feng, K. Knapp, Y. Luo, R. Mendoza, V. Patel, M. Tuszeowski, and A. D. Van Drie, *Rev. Sci. Instrum.* **83**, 10D709 (2012).

²⁸D. Osin, D. Gupta, S. Korepanov, M. Onofri, S. Gupta, and S. Detrick, *Bull. Am. Phys. Soc.* **58**, GP8.00040 (2013).

²⁹D. K. Gupta, B. H. Deng, K. Knapp, X. Sun, and M. C. Thompson, *Rev. Sci. Instrum.* **83**, 10D534 (2012).

³⁰D. K. Gupta, E. Paganini, A. Balvis, L. Bonelli, B. H. Deng, F. Giannanco, O. Gornostaeva, R. Hayashi, K. Knapp, P. Marsili, M. McKenzie, R. Pousa-Hijos, S. Primavera, J. Schroeder, and M. Tuszeowski, *Rev. Sci. Instrum.* **81**, 10D737 (2010).

³¹D. Osin, J. Douglass, and M. Tuszeowski, *Bull. Am. Phys. Soc.* **59**, UP8.00016 (2014).

³²J. Douglass, *Bull. Am. Phys. Soc.* **55**, GP9.00096 (2010).

³³S. Korepanov, A. Smirnov, R. Clary, S. Detrick, P. Deichuli, A. Kondakov, and S. Murakhtin, *Rev. Sci. Instrum.* **83**, 10D720 (2012).

³⁴R. Clary, A. Smirnov, S. Detrick, K. Knapp, S. Korepanov, E. Ruskov, W. W. Heidbrink, and Y. Zhu, *Rev. Sci. Instrum.* **83**, 10D713 (2012).

³⁵E. Ruskov, M. Tuszeowski, Y. Zhu, and W. Heidbrink, *Bull. Am. Phys. Soc.* **55**, GP9.00103 (2010); E. Garate, I. Allfrey, T. Valentine, V. Patel, A. Smirnov, S. Korepanov, R. Clary, and M. Thompson, *ibid.* **57**, PP8.00045 (2012).

056110-16 Binderbauer *et al.*

Phys. Plasmas 22, 056110 (2015)

- ³⁶R. M. Magee, R. Clary, S. Korepanov, A. Smirnov, E. Garate, K. Knapp, and A. Tkachev, *Rev. Sci. Instrum.* **85**, 11D851 (2014).
- ³⁷B. H. Deng, J. S. Kinley, K. Knapp, P. Feng, C. Weixel, S. Armstrong, R. Hayashi, A. Longman, R. Mendoza, H. Gota, and M. Tuszeowski, *Rev. Sci. Instrum.* **85**, 11D401 (2014).
- ³⁸L. Schmitz, E. Ruskov, B. H. Deng, H. Gota, D. Gupta, M. Tuszeowski, J. Douglas, W. A. Peebles, M. Binderbauer, and T. Tajima, *Rev. Sci. Instrum.* **85**, 11D840 (2014).
- ³⁹T. Roche, X. Sun, S. Armstrong, K. Knapp, and M. Slepchenkov, *Rev. Sci. Instrum.* **85**, 11D824 (2014).
- ⁴⁰H. Gota, M. C. Thompson, K. Knapp, A. D. Van Drie, B. H. Deng, R. Mendoza, H. Y. Guo, and M. Tuszeowski, *Rev. Sci. Instrum.* **83**, 10D706 (2012).
- ⁴¹K. Zhai, J. Kinley, H. Zhang, and B. LeBlanc, Bull. Am. Phys. Soc. **59**, UP8.00007 (2014).
- ⁴²D. Gupta, E. Granstedt, S. Gupta, R. Magee, D. Osin, and M. Tuszeowski, Bull. Am. Phys. Soc. **59**, UP8.00014 (2014).
- ⁴³D. Stotler and C. Karney, *Contrib. Plasma Phys.* **34**, 392 (1994).
- ⁴⁴M. Thompson, R. Clary, S. Korepanov, A. Longman, A. Sibley, A. Smirnov, and M. Tuszeowski, Bull. Am. Phys. Soc. **57**, PP8.00041 (2012); R. Magee, R. Clary, S. Detrick, S. Korepanov, M. Onofri, and A. Smirnov, Bull. Am. Phys. Soc. **58**, GP8.00043 (2013).
- ⁴⁵S. Gupta, S. Detrick, and D. C. Barnes, Bull. Am. Phys. Soc. **56**, CP9.00094 (2011); S. Gupta, S. Detrick, and D. Barnes, *ibid.* **58**, GP8.00049 (2013); S. Gupta, S. Detrick, D. Barnes, T. Tajima, and E. Trask, Bull. Am. Phys. Soc. **59**, UP8.00070 (2014).
- ⁴⁶M. N. Rosenbluth and M. N. Bussac, *Nucl. Fusion* **19**, 489 (1979); D. Barnes, C. Seyler, and D. Anderson, in *Proceedings of US-Japan Joint Symposium on Compact Toruses and Energetic Particle Injection*, Princeton, NJ, 1979 (Princeton Plasma Physics Laboratory, Princeton University, 1979), p. 110; J. Hammer, *Nucl. Fusion* **21**, 488 (1981).
- ⁴⁷S. Ohi, T. Minato, Y. Kawakami, M. Tanjyo, S. Okada, Y. Ito, M. Kako, S. Goto, T. Ishimura, and H. Ito, *Phys. Rev. Lett.* **51**, 1042 (1983).
- ⁴⁸A. Smirnov, S. Detrick, R. Clary, S. Korepanov, M. Thompson, E. Trask, and M. Tuszeowski, Bull. Am. Phys. Soc. **57**, PP8.00042 (2012).
- ⁴⁹F. Zhong, Y. Petrov, and T. Huang, *Phys. Plasmas* **11**, L1 (2004).
- ⁵⁰A. W. Carlson, *Phys. Fluids* **30**, 1497 (1987).
- ⁵¹J. Wesson, *Tokamaks*, 4th ed. (Oxford University Press, Oxford, UK, 2011), p. 180.
- ⁵²D. Fulton, C. Lau, I. Holod, Z. Lin, S. Detrick, M. Binderbauer, and T. Tajima, Bull. Am. Phys. Soc. **59**, UP8.00006 (2014).
- ⁵³S. M. Kaye, F. M. Levinton, D. Stutman, K. Tritz, H. Yuh, M. G. Bell, R. E. Bell, C. W. Domier, D. Gates, W. Horton, J. Kim, B. P. LeBlanc, N. C. Luhmann, Jr., R. Maingi, E. Mazzucato, J. E. Menard, D. Mikkelsen, D. Mueller, H. Park, G. Rewoldt, S. A. Sabbagh, D. R. Smith, and W. Wang, *Nucl. Fusion* **47**, 499 (2007); S. M. Kaye, S. Gerhardt, W. Guttenfelder, R. Maingi, R. E. Bell, A. Diallo, B. P. LeBlanc, and M. Podesta, *ibid.* **53**, 063005 (2013).
- ⁵⁴L. Schmitz, B. Deng, H. Gota, T. Tajima, D. Gupta, J. Douglass, M. Binderbauer, and E. Ruskov, Bull. Am. Phys. Soc. **59**, UP8.00013 (2014).
- ⁵⁵Y. Kishimoto, J.-Y. Kim, T. Fukuda, S. Ishida, T. Fujita, T. Tajima, W. Horton, G. Furnish, and M. J. LeBrun, in *Proceedings of the 6th IAEA Fusion Energy Conference, Montreal, 1996* (International Atomic Energy Agency, Vienna, 1997), Vol. 2, p. 581; Y. Kishimoto, T. Tajima, W. Horton, M. J. LeBrun, and J.-Y. Kim, *Phys. Plasmas* **3**, 1289 (1996).
- ⁵⁶T. Matsumoto, J. Sekiguchi, T. Asai, H. Gota, E. Garate, I. Allfrey, T. Valentine, B. Smith, and M. Morehouse, Bull. Am. Phys. Soc. **59**, UP8.00008 (2014).

